ACS APPLIED MATERIALS & INTERFACES

Article

Polydopamine-Coated Manganese Carbonate Nanoparticles for Amplified Magnetic Resonance Imaging-Guided Photothermal Therapy

Youxing Cheng, Shupeng Zhang, Ning Kang, Jianpan Huang, Xiaolin Lv, Kai Wen, Shefang Ye, Zhiwei Chen, Xi Zhou, and Lei Ren

ACS Appl. Mater. Interfaces, **Just Accepted Manuscript** • Publication Date (Web): 16 May 2017

ACS Publications

ACS Applied Materials & Interfaces is published by the American Chemical Society. 1155 Sixteenth Street N.W., Washington, DC 20036

Polydopamine-Coated Manganese Carbonate Nanoparticles for Amplified Magnetic Resonance Imaging-Guided Photothermal Therapy

Youxing Cheng, [a] *Shupeng Zhang,* [a] *Ning Kang,* [a] *Jianpan Huang,* [d] *Xiaolin Lv,* [a] *Kai Wen,* [a] *Shefang Ye,* [a] *Zhiwei Chen,* [d]* *Xi Zhou* [a]* *and Lei Ren* [a,b,c]

a Department of Biomaterials, College of Materials, Xiamen University, Xiamen 361005, Fujian, P. R. China

b Fujian Collaborative Innovation Center for Exploitation and Utilization of Marine Biological Resources, Xiamen University, Xiamen 361005, Fujian, P. R. China

c State Key Laboratory of Physical Chemistry of Solid Surface, School of Chemistry and Chemical Engineering, Xiamen University, Xiamen 361005, Fujian, P. R. China

d Department of Electronic Science, College of Physical Science and Technology, Fujian Provincial Key Laboratory of Plasma and Magnetic Resonance Research, Xiamen University, Xiamen 361005, Fujian, P. R. China

ABSTRACT:

This study reports a multifunctional nanoparticle (NP) with function of amplified magnetic resonance image (MRI)-guided photothermal therapy (PTT) by the surface coating of polydopamine (PDA) shell. Importantly, by means of introducing the surface coating of PDA, it helps entrap large quantities of water around NPs and allow more efficient water exchange, leading to greatly improved MR contrast signals compared with the one without PDA coating. Besides, the distinct photothermal effect can be obtained arising from the strong absorption of PDA in the near-infrared (NIR) region. By synthesizing the multifunctional $MnCO_3$@PDA NPs as example, we found that the longitudinal relaxivity (r_1) of $MnCO_3$ NPs might improve from 5.7 to 8.3 $mM^{-1}s^{-1}$. Subsequently, In vitro MRI and PTT results verified that $MnCO_3$@PDA could serve well as an excellent MRI/PTT theranostic agent. Furthermore, the $MnCO_3$@PDA nanoparticles were applied as MRI/PTT theranostic agent for in vivo MRI-guided photothermal ablation of tumors by intratumorally injection in 4T1 tumor bearing-mice. The MR imaging result shows a significantly bright MR image in the tumor site. The $MnCO_3$@PDA-mediated PTT result shows high therapy efficiency as a result of their high photothermal conversion efficiency. The present strategy of amplified MRI-guided PTT based on PDA coating on NPs will be widely applicable to other multifunctional nanoparticles.

KEYWORDS: Manganese carbonate, Polydopamine, Multifunctional, Magnetic resonance imaging, Photothermal therapy

1. INTRODUCTION

It is well-known that multifunctional nanocomplexes have attracted great attention in the biomedical fields because of their combined features of diagnostic sensing and therapeutic

functions within a single platform.[1-4] The simple synthesis procedures and commercially available raw materials for various nanocomplexes, including Janus particles, core/shell nanoparticles and element doped nanoparticles (NPs), further stimulated the development of theranostic nanomedicine due to facilitated clinical translation.[5-8] To date, a large number of theranostic agents have been created by combining diagnostic functions such as magnetic resonance imaging (MRI), photoacoustic imaging (PA) and X-ray computed tomography (CT) with therapeutic roles such as radiotherapy, chemotherapy and photothermal therapy (PTT), for potential applications in cancer or other diseases.[9-12] The nanocomplex with MRI and PTT functions has especially drawn much attention for its intrinsic characteristics that combine the high spatial resolution, noninvasiveness and three-dimensional images of MRI and the noninvasiveness, low side effects, high efficiency and selectivity of PTT.[13-16]

Manganese-based nanoparticulate systems (such as MnO, $MnSiO_3$, Mn_3O_4 etc.), have been extensively studied as candidates for MRI T_1-weighted contrast agents due to their efficient positive contrast enhancement effects.[17-19] It is also established that these multifunctional theranostic agents are exploited from manganese-based particles through hybridization or integration. For instance, manganese oxide and small molecules, such as doxorubicin, protoporphyrin and gene agents, have been successfully integrated into a nanoplatform to establish T_1 MRI-guided tumor chemotherapy and photodynamic therapy (PDT).[20-22] In addition, Mn-based MR contrast agents could be combined with photothermal materials (e.g. carbon, iron oxide or copper sulfide) for theranostic applications.[23-25] However, Mn-based nanoparticles usually suffer from a poor relaxation rate and low-efficiency MRI performance. Especially, the relaxation rate will further decrease when these nanoparticles are functionalized with most types of materials (e.g. mesoporous silica and gold NPs).[26-27] Until now, several strategies have been

suggested to improve the relaxation rate of manganese-based nanoparticles. An effective way is to modulate the morphology of the manganese-based nanoparticles and provide large water-accessible surface areas. For instance, MnO nanoparticles with hollow structure and plate-like morphology exhibit r_1 (relaxation rate) values of 1.417 $mM^{-1}s^{-1}$ and 5.5 $mM^{-1}s^{-1}$ respectively, which are more than 6-fold and 21-fold higher than that of their spherical counterparts.[28-29] Alternatively, Chen *et al*. reported that the surface coating of human serum albumin (HSA) could enhance the r_1 relaxivity of MnO NPs to 1.97 $mM^{-1}s^{-1}$, which makes HSA-MnO nanoparticles perform prominently in MRI/PET dual imaging.[30] Nonetheless, these relaxivities are still far smaller than that of clinical T_1 contrast agents such as Gadolinium-DTPA. Although Ye *et al.* obtained a higher r_1 relaxivity of 6.81 $mM^{-1}s^{-1}$ by doping Gadolinium (Gd) in $MnCO_3$ and achieved multifunctional MR/fluorescence imaging of tiny brain gliomas, translating their findings in practice has been hampered by the serious toxic side effects, such as nephrogenic systemic fibrosis, caused by the liberation of Gd ions from nanoparticles.[26, 31] Therefore, it remains a great challenge to acquire biocompatible manganese-based theranostic agents with a high MR contrast effect.

Polydopamine (PDA) has been widely applied in the biomedical fields due to its outstanding biocompatibility and good biodegradability.[32-35] Besides the distinct photothermal therapeutic properties arising from its strong absorption in the near-infrared (NIR) region,[32, 36-39] the inherently loose structure,[32, 40-41] stable π-electron free radical species[32] and high hydrophilicity[32] of PDA make it a suitable material for entrapping large quantities of water around NPs and allow more efficient water exchange. Thus, due to the excellent advantages of PDA coating, it is possible to enhance the MR contrast of manganese-based nanoparticles, as well as additional functions for PTT. On the other hand, $MnCO_3$ offers fascinating properties such as being more

sensitive to acidic conditions for their inherent nature of composition with Mn^{2+} and CO_3^{2-} as well as no long-term toxicity caused by accumulation of NPs compared to other manganese-based MR contrast agents.[42] Therefore, we designed and manufactured multifunctional $MnCO_3$@PDA core-shell nanocomposites for potential MRI/PTT theranostic agent. Benefiting from surface coating with PDA, the prepared $MnCO_3$@PDA core/shell nanocomposites showed low cell toxicity, and the longitudinal relaxivity was enhanced from 5.7 $mM^{-1}s^{-1}$ to 6.3 $mM^{-1}s^{-1}$ at pH 7.4 using the 7T MRI system. Furthermore, in acidic conditions (pH 6.0), the longitudinal relaxivity further increased to 8.3 $mM^{-1}s^{-1}$. Subsequently, *In vitro* MRI and PTT results verified that $MnCO_3$@PDA could serve well as an excellent MRI/PTT theranostic agent. Moreover, the $MnCO_3$@PDA nanoparticles were applied as MRI/PTT theranostic agent for *in vivo* MRI-guided photothermal ablation of tumors by intratumorally injection in 4T1 tumor bearing-mice. This nanoformulation enables high-resolution tumor imaging of small animals by MRI. The $MnCO_3$@PDA-mediated PTT result shows high therapy efficiency as a result of their high photothermal conversion efficiency. Our proposed strategy suggests an amplified MRI-guided PTT based on PDA coating on NPs, which can be potentially applied in early tumor diagnosis and therapy.

2. EXPERIMENTAL SECTION

2.1. Materials

Manganese chloride tetrahydrate ($MnCl_2 \cdot 4H_2O$), ammonium carbonate ($(NH_4)_2CO_3$), hydrochloric acid, nitric acid, ethanol, sodium carbonate (Na_2CO_3) and tris(hydroxymethyl) aminomethane (Tris) were purchased from Shantou Xilong Chemical Factory (Guangdong, China). Cyltrimethylammonium bromide (CTAB), cyclohexane, pentanol, poly (acrylic acid) (PAA, mw = 3000) and dimethylsulfoxide (DMSO) were obtained from Sinopharm Chemical

Reagent Co. Ltd. (Shanghai, China). Dopamine hydrochloride (98 %), Polyetherimide (PEI, mw = 600) was purchased from Aladdin Industrial Corporation. Dulbecco's modified eagle medium (DMEM), Roswell Park Memorial Institute (RPMI) 1640, penicillin-streptomycin and phosphate buffered saline (PBS) were purchased from Biological Industries (Beit Ahemeq, Israel). Fetal bovine serum (FBS) and trypsin were purchased from Invitrogen (USA). Calcein-acetoxymethyl (calcein-AM), propidium iodide (PI), fluorescein isothiocyanate (FITC) and 3-(4, 5-Dimethylthiazol-2-yl)-2, 5-diphenyltetrazolium bromide (MTT) were purchased from Nanjing KeyGen Biotech Co. Ltd. (Nanjing, China). All chemicals were used without further purification. Ultrapure water (18.2 MΩ·cm) were obtained from Milli-Q Water Purification System.

2.2. Synthesis of $MnCO_3$ NPs

The $MnCO_3$ NPs were prepared using microemulsion mediated route reported by Hu's group[43]. In a typical procedure, 0.792 g of $MnCl_2 \cdot 4H_2O$ was dissolved in 8 mL of water named as solution A, and 0.384 g of $(NH_4)_2CO_3$ was dissolved in 8 mL of water named as solution B. Then, 4 g of CTAB was added into a 250 mL beakerflask containing 50 mL of cyclohexane, 4 mL of pentanol and 0.6 mL of solution A. The mixture was stirred at room temperature until it become transparent. At last, 0.6 mL of solution B was added dropwise into the beaker flask under magnetic stirring for an hour. Finally, the $MnCO_3$ NPs were separated by centrifugation (8000 rpm, 5 min), washed with ethanol for twice and water for three times. The as-synthesized 35 mg of $MnCO_3$ NPs was re-dispersed in 3.5 mL water and stored at 4 °C with a concentration of 10 mg/mL for further use.

2.3 Preparation of PAA Modified $MnCO_3$ NPs

A certain amount of PAA (0.03 mmol) was added into 90 mL water and Na_2CO_3 (0.5 M) was used to adjust pH to 8.0 to obtain PAA-Na. The prepared PAA-Na (2.5 mL) solution was added into 80 mL water containing 20 mg $MnCO_3$ NPs. And the mixture was stirred for 4 h at room temperature. After centrifugation (12000 rpm, 5 min), the product was washed with water for three times and the obtained 15 mg of $MnCO_3$-PAA NPs were re-dispersed in 3 mL water with a concentration of 5 mg/mL for further use.

2.4 Preparation of $MnCO_3$@PDA NPs

2.5 mg of PAA modified $MnCO_3$ NPs were dispersed in 30 mL Tris-HCl buffer solution (pH ~ 8.5) and then 2.0 mg of dopamine hydrochloride was added into the reaction system under sonication for 30 min followed by an additional shaking for 4 h. To get rid of the unreacted material, the solution was centrifuged for 5 min at 12000 rpm and the obtained $MnCO_3$@PDA NPs were washed with water for three times. The obtained 3 mg of $MnCO_3$@PDA NPs were dispersed in 5 mL water with a concentration of 0.6 mg/mL for the following characterization.

2.5 Characterization

Powder X-ray diffraction (XRD) patterns were recorded on powder XRD system (Philips P analytical X'pert PRO) equipped with Cu K_α radiation (λ = 1.542 nm) over the 2θ range of 20-60°. Morphological characterizations were performed using scanning electron microscopy (SEM, SU70, Japan) and transmission electron microscopy (TEM, JEOL JEM-2100, Japan). High-resolution TEM, selected area electron diffraction (SAED), high-angle annular dark-field scanning transmission electron microscopy (HAADF-STEM), energy-dispersive X-ray spectroscopy (EDS) elemental mapping and line-profile elemental analysis were performed using a Talos F200 S/TEM microscope (FEI Company) operated at 200 kV. The surface compositions of the samples were further determined by X-ray photoelectron spectra (XPS) performed on a

Qtac-100 LEISSXPS Instrument. Thermogravimetric (TG) analysis was performed with a Netzsch TG 209F1 instrument both in an N_2 and air atmosphere at a heating rate of 10 °C/min. The hydrodynamic radius and zeta potential distribution of NPs dispersed in water were measured on a Malvern Zetasizer Nano ZS (Malvern Instruments Ltd., Worchestershire, U.K.). The Fourier Transform Infrared (FTIR) spectra were recorded on a Nicolet iS10 (Thermo Scientific, USA) with KBr pellet technique. UV/Vis absorption spectra were acquired with a UV spectrophotometer (UV-1750, Shimadzu, Japan). T_1 relaxation time and in vivo MR images measurements were recorded at 25 °C using a 7T Bruker Biospec small animal MRI system (Bruker, Inc., Billerica, MA). The concentration of Mn^{2+} was determined by inductively coupled plasma mass spectrometry (ICP-MS, Perkin-Elmer, USA).

2.6. Manganese Ion Release Behavior of $MnCO_3$@PDA

$MnCO_3$@PDA NPs (100 μL, 500 μg/mL) were dispersed in 3 mL PBS (pH 7.4 / 6.0) at different time intervals and followed by centrifugation (12000 rpm, 3 min). The supernatants were harvested and diluted with 3 % of nitric acid for ICP test.

2.7. MR Contrast Measurements

$MnCO_3$ and $MnCO_3$@PDA NPs (in pH 7.4 / 6.0 for 2 h) were dispersed in 1 % agarose with different Mn^{2+} concentrations (by ICP-MS measurement) in the range of 0-0.2 mM. By using the T_1 RARE sequence to acquire T_1-weighed MR images and T_1 relaxation time: TR (repetition time) = 800 ms, TE (echo time) = 10 ms, average times = 4, slice thickness = 0.5 mm, FOV (field of view) = 2.5×2.5, matrix = 256×256. T_1 relaxation rates were plotted against the Mn^{2+} concentrations and the relaxivity was determined by a linear fit.

2.8. Photothermal Effect Measurements of $MnCO_3$@PDA

$MnCO_3$@PDA NPs with different mass concentrations (0.1, 0.2, 0.3 mg/mL) were irradiated by NIR laser exposure (808 nm, 2 W/cm^2) in 2 mL test tube. 0.3 mg/mL of $MnCO_3$ NPs were also irradiated by the same NIR laser for comparison with water as control. IR thermal camera (FLIR-Systems A35, Sweden) was used to obtain images and record the data of temperatures. In addition, photothermal stability of $MnCO_3$@PDA NPs was also investigated by continuously 10 min irradiation, dropping to room temperature, followed by another 10 min irradiation for total three cycles.

2.9. Cell and Animal Models

Human cervical carcinoma cells (HeLa) and 4T1 murine breast cancer cells (4T1) were originally obtained from American Type Culture Collection (ATCC) and cultured under recommended medium (DMEM / 1640 supplemented with 1 % penicillin / streptomycin and 10 % FBS) at 37 °C within 5 % CO_2 atmosphere. Female BALB/c mice were obtained from Beijing Vital River Laboratories Animal Technology Co. Ltd. and used under protocols approved by Institutional Animal Care and Use Committee of Xiamen University. The 4T1 tumor models were obtained by subcutaneous injection of 2×10^6 cells into the right abdomen of each female BALB/c mouse.

2.10. Cell Viability Assay of $MnCO_3$ and $MnCO_3$@PDA NPs

The standard MTT assay was carried out to evaluate the *in vitro* cytoviability of $MnCO_3$ and $MnCO_3$@PDA NPs. Namely, Both HeLa cells and 4T1 cells (1×10^4 cells per well) were allowed to adhere for 12 h before adding NPs ($MnCO_3$ or $MnCO_3$@PDA). After that, six different grade concentrations (0, 0.01, 0.05, 0.10, 0.20, 0.30 mg/mL) of the NPs dispersed in fresh medium were added into the cells and incubated at 37 °C for another 24 h. After that, cells were washed with PBS for three times, followed by addition of fresh medium with aliquots of MTT (20 μL, 5

mg/mL) and incubated for another 4 h. After removing the medium, 150 μL DMSO was added into each well and the plate was shook gently for 15 min. The absorbance of purple formazan was measured at 570 nm by using a spectrophotometric microplate reader (BioRad 680, Hercules, CA, USA). For the study of toxicity caused by Mn^{2+} and CTAB, HeLa cells (1×10^4 cells per well) were allowed to adhere for 12 h and then incubated with fresh medium contained $MnCl_2$ (0, 30, 150, 300 and 600 μM) and CTAB (0, 0.04, 0.08, 0.8, 1.6 and 2.4 μM) for another 24 h and then examined the cell viability by standard MTT assay.

2.11. Cell Uptake of $MnCO_3$ and $MnCO_3$@PDA NPs

HeLa cells were seeded into 12-well plates (1×10^6 cells per well) until adhesion for 12 h. For cell uptake of $MnCO_3$ NPs, $MnCO_3$ NPs were modified with PEI and then connected with FITC for further use.[10] Afterwards, 1 mL fresh medium containing 100 μg FITC labeled $MnCO_3$-PEI NPs was added into the plate and incubated with HeLa cells for 12 h. After that, the cells were photographed on a Zeiss LSM 5 exciter (Carl Zeiss AG, Jena, Germany) confocal laser scanning microscope. For cell uptake of $MnCO_3$@PDA NPs, 1 mL fresh medium containing 100 μg FITC labeled $MnCO_3$@PDA NPs was added into each plate at different time intervals (1, 2, 4, 8, 12 h). Cells treated with fresh medium were served as a negative control group. Cells were digested with trypsin for 3 min and suspended in 100 μL PBS. The fluorescence intensity of cells was measured on a Beckman Coulter Cell Lab Quanta SC with excitation wavelengths of 488 nm.

2.12. In Vitro Photothermal Effect

The photothermal treatment effect of $MnCO_3$@PDA NPs was determined by using a standard MTT assay and live/dead dual staining assay. For MTT assay, HeLa cells and 4T1 cells were seeded in 96-well plates at a density of 1×10^4 cells per well and cultured at 37 °C for 12 h. Then, the cells were incubated with different grade concentrations of NPs for another 12 h before being

exposed to an 808 nm laser (2 W/cm^2, 10 min). Afterward, the standard MTT assay was carried out to evaluate the cell viability.

For live/dead dual staining, HeLa cells were seeded in 24-well plates at a density of 1×10^5 cells per well and cultured at 37 °C for 12 h. Then, the cells were divided into four groups as control, NIR laser, $MnCO_3$@PDA and $MnCO_3$@PDA +NIR. HeLa cells were incubated with and without $MnCO_3$@PDA (0.1 mg/mL) for 8 h and then irradiated with 808 nm laser for 10 min at 2 W/cm^2 followed by incubating for another 30 min. Finally, fresh mediums containing calcein-AM and PI were applied to stain the cells before being photographed by an inverted fluorescence microscope (Axiovert 200, Zeiss).

2.13. In Vivo MR imaging

In vivo MR imaging was performed on an anesthetized healthy BALB/c white mouse bearing $4T_1$ tumors after intratumorally injection of 50 μL (100 μg/mL) $MnCO_3$@PDA NPs using a T_1-weighted sequence (MESE): TR = 400 ms, TE = 15 ms, average times = 1, slice thickness = 2 mm, FOV (field of view) = 4×4, matrix = 256×256. The MR images were obtained at pre-injection and post-injection of $MnCO_3$@PDA NPs at 15 min, 30 min, 50 min, 70 min, 90 min and 120 min.

2.14. In Vivo Photothermal Therapy

In vivo photothermal ablation experiment was carried out on 4T1 tumor-bearing BALB/c mice by intratumoral injection of 50 μL (500 μg/mL) of $MnCO_3$@PDA NPs. The mice had been randomly distributed into four groups (4 mice in each group) named as PBS; PBS + NIR; $MnCO_3$@PDA and $MnCO_3$@PDA + NIR. The tumor volume was calculated by the formula of $V = L\times W^2/2$, where V, L and W represent the volume, length and width of the tumor, respectively. The laser irradiation was performed using an 808 nm NIR laser with a power

density of 1.4 W/cm^2 for 6 min. During the treatment, an IR thermal camera was used to obtain pictures of all mice and record their real-time temperature change at tumor site. The tumor sizes and body weights were measured every 2 days. Relative tumor volumes were obtained by dividing the initial tumor size before laser treatment. After treatment on 14th day, the mice were euthanized and tissues including heart, liver, spleen, lung, kidneys and tumor were harvested for further histological examinations by the hematoxylin and eosin (H & E) staining.

3. RESULTS AND DISCUSSION

3.1. Synthesis and Characterization of $MnCO_3$ and $MnCO_3$@PDA NPs

The synthetic process of $MnCO_3$@PDA NPs was illustrated in scheme 1. Firstly, $MnCO_3$ nanoparticles were fabricated through microemulsion mediated method, as reported by Hu's group with a slight modification[43]. Second, PAA bound to the surface of $MnCO_3$ NPs through the strong affinity between the carboxy group and metal ions. Finally, dopamine adsorbed onto the surface of $MnCO_3$-PAA NPs via electrostatic interactions between -COO and -NH_2 groups[44], and then self-polymerized to form $MnCO_3$@ PDA.

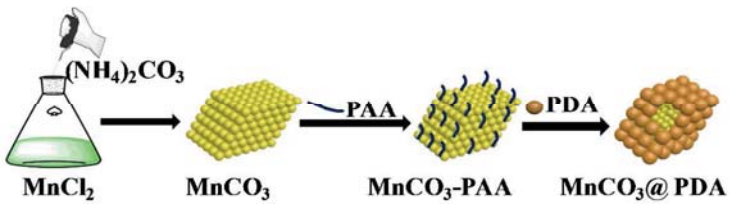

Scheme 1. Schematic illustration of the synthesis of of $MnCO_3$@PDA nanocomposites.

Powder XRD tests were employed to confirm the crystalline structures of the as-prepared $MnCO_3$ NPs. Figure 1A showed that all peaks of the NPs matched well with the pure rhombohedral phase of $MnCO_3$ powder (JCPDS No. 44-1472). There were no other peaks of impurities originating from manganese oxides in XRD data, demonstrating the homogeneous $MnCO_3$ nanocrystals obtained in the experiment. The morphology and intrinsic crystal structures

of the as-synthesized $MnCO_3$ NPs were also confirmed by SEM and TEM/HRTEM. As shown in Figure 1B (Figure S1 and Figure S2a), the as-prepared $MnCO_3$ NPs exhibited a tridimensional rhomboid shape with relative uniform size and the side length was about 100 nm. Close inspection of an individual $MnCO_3$ particle (Figure 1D) revealed the lattice fringe spacing to be 0.287 nm, matching the (104) diffraction plane of the rhombohedral structure of $MnCO_3$. Moreover, the diffraction dots in the selected area electron diffraction (SAED) pattern (Figure S3) showed a single crystalline property as well as the highly crystalline nature of NPs, which was corresponding to the XRD results. The atomic compositions of as synthesized $MnCO_3$ NPs were confirmed by STEM EDS elemental mapping and line-profile elemental (Mn, C, O, N) analysis (Figure 1E and 1F). The surface atomic composition of $MnCO_3$ NPs had also been further confirmed by XPS analysis (Figure S4a and S4b) with only a weak peak appeared at a binding energy of 398.2 eV for $MnCO_3$ NPs. These results showed that in the progress of synthesizing $MnCO_3$ NPs, the CTAB molecules had absorbed on the surface of NPs with a low content. Additionally, the quantification of CTAB was determined by TG analysis under N_2 atmosphere. As shown in Figure S5a, the weight loss of CTAB molecules was 100 wt% when the temperature increased from 35 °C to 750 °C, indicating that CTAB decomposed completely. During the same period of temperature, the weight loss of pure $MnCO_3$ NPs (synthesized by mixing $MnCl_2$ and $(NH_4)_2CO_3$ solutions) and $MnCO_3$-CTAB NPs (as-prepared $MnCO_3$ NPs) were 56.8 wt%and 55.9 wt% respectively, indicating that about 0.9 wt% of CTAB remaining on the NPs.

The zeta potential of as-prepared $MnCO_3$ NPs was measured at +28.7 mV, attributed to the coexistence of Mn^{2+} and CTAB on the surface of particles (Figure 1G). However, the mean hydrodynamic radius of the $MnCO_3$ NPs was 498 nm (Figure 1H), five times larger than the size measured by TEM (100 nm) result. This was ascribed to the aggregation of positively charged

$MnCO_3$ NPs. The stability of $MnCO_3$ NPs was further recorded by dynamic light scattering (DLS) and zeta potential (Figure S6a). The hydrodynamic radius of the $MnCO_3$ NPs increased as time went on, while the final Zeta potential trend to arrive at 0 mV. This result showed the $MnCO_3$ NPs without much CTAB were not stable in water. Therefore, based on the high affinity between -COO and Mn^{2+}, PAA ligands were applied to modify $MnCO_3$ NPs to improve the dispersibility. After being modified with PAA molecules, the morphology of $MnCO_3$ NPs seemed to be etched and the surface became smooth without sharp corner (Figure S2b). Meanwhile, the conjunction of PAA and $MnCO_3$ had been verified by the zeta potential analysis with a negative value of -13.4 mV (Figure 1G). Finally, $MnCO_3$@PDA core/shell NPs were obtained by self-polymerization of dopamine on the surface of PAA-modified $MnCO_3$ NPs. The irregular PDA shell could be observed on the surface of $MnCO_3$ NPs, leading to a size increase of nanocomplex (about 140 nm) determined by TEM image (Figure 1C and Figure S2c). Attributed to the existence of catechol groups in PDA, the final zeta potential value arrived at -18.1 mV, ensuring an excellent colloidal stability of nanoparticles. And the hydrodynamic diameter of $MnCO_3$@PDA decreased to 173 nm (Figure 1H), which was a little larger than the TEM results for the reason that the size of NPs determined by DLS was the sum of the core size and the thickness of surrounded water molecules[45]. Compared with $MnCO_3$ NPs, both the hydrodynamic radius and Zeta potential showed no much change within 48 h (Figure S6b), indicating a high colloidal stability and dispersibility.

Furthermore, the surface coating of $MnCO_3$ NPs with PDA was investigated by FT-IR absorption spectroscopy and XPS spectra. As shown in Figure 1G, all $MnCO_3$-based nanomaterials had a main absorption band around 1440 cm^{-1} (vs), 860 cm^{-1} (m), 720 cm^{-1} (w) which were assigned to the CO_3^{2-}.[46] The weakened absorption peaks at 2917 cm^{-1} and 2849 cm^{-1}

were the stretching vibration of -C-H in $-CH_2-$ and $-CH_3$, further indicating that only a few CTAB remained on the surface of $MnCO_3$. The successful modification of PDA was the appearance of the variations of the characteristic functional groups at 1577 cm^{-1} (the benzene skeleton vibration of PDA).[47-48] Additionally, XPS analysis $MnCO_3$@PDA (Figure S4a and S4b), showed an obvious peak of the element N on the spectra, indicating the successful coating of PDA on the surface of $MnCO_3$. And the amount of PDA shell was about 20 wt% which was determined by TG analysis (Figure S5b).

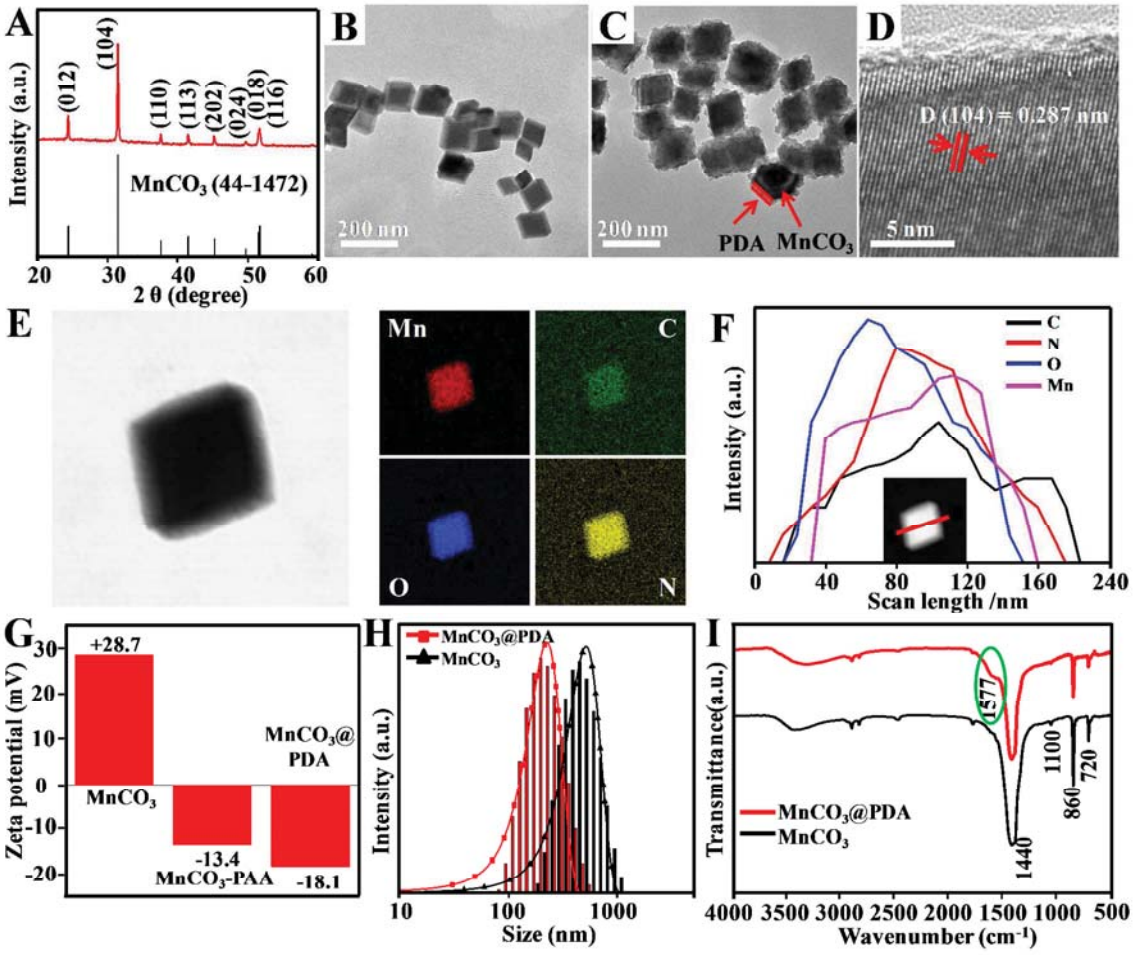

Figure 1. Characterization of $MnCO_3$ and $MnCO_3$@PDA NPs: (A) XRD pattern and (B) TEM image of $MnCO_3$; (C) TEM image of $MnCO_3$@PDA; HRTEM image (D) STEM and EDX

elemental mapping (E) and line-profile elemental analysis (F) of $MnCO_3$ NPs; (G) The Zeta potential change of $MnCO_3$, $MnCO_3$-PAA and $MnCO_3$@PDA NPs dispersed in water. (H) Hydrodynamic particle size of $MnCO_3$ and $MnCO_3$@PDA NPs in water. (I) FT-IR spectra of $MnCO_3$ and $MnCO_3$@PDA nanocomplex.

3.2. Manganese Ion Release Behavior and MR Contrast Capabilities of NPs

With the intention of imitating the Mn^{2+} release behavior of $MnCO_3$@PDA in the microenvironment inside and outside of cells, we conducted the following experiment by measuring Mn^{2+} release at pH 7.4 and 6.0, which stand for the physiological environments and the low pH endosome, respectively.[49-50] The released Mn^{2+} from $MnCO_3$@PDA nanocomposites under different pH (6.0 and 7.4) were determined using ICP analysis (Figure 2A). Obviously, acidic aqueous (pH 6.0) could promote the release of Mn^{2+} up to 70 %, comparing with only 8 % for NPs under pH 7.4. The small quantity of Mn^{2+} release in neutral environment (pH 7.4) is possibly due to the hydrolysis of $MnCO_3$ at room temperature. While the large amount of released Mn^{2+} can be explained by the accelerated ionization of $MnCO_3$ in acidic condition.[42, 51]

It has been proved that Mn^{2+} with five unpaired electrons is an effective T_1 contrast agent in MR imaging. In order to confirm MR contrast capabilities and reveal the effect of PDA on the MR performance of $MnCO_3$ NPs, T_1 signal of $MnCO_3$ and $MnCO_3$@PDA NPs at pH 7.4 and 6.0 were carried out using on 7T small animal MR scanner (Figure 2B). The r_1 value of the $MnCO_3$ in near neutral solutions (pH 7.4) was calculated to be 5.7 $mM^{-1}s^{-1}$, and it became 6.3 $mM^{-1}s^{-1}$ after coating with PDA shell, showing a r_1 value increased by 0.6 $mM^{-1}s^{-1}$. Meanwhile, the r_1 value of $MnCO_3$ and $MnCO_3$@PDA NPs was further increased in the presence acidic buffer (pH 6.0). However, the r_1 was enhanced from 6.9 $mM^{-1}s^{-1}$ to 8.3 $mM^{-1}s^{-1}$, indicating that PDA shell can exhibit a positive MR contrast enhancement. These were attributed to the following reasons:

(1) high hydrophilicity of PDA shell prevent the aggregation of $MnCO_3$ NPs and provide a water-accessible surface areas;[28] (2) the inherently loose structures and stable π-electron free radical species of PDA accelerate the exchange rate between water protons and Mn^{2+}, resulting the enhancement of r_1.[32] Additionally, the bright intensity of their T_1-weighted images (Figure 2C) was increased with an increase in Mn^{2+} ion concentration, showing a Mn concentration dependent manner. Compared with $MnCO_3$, the T_1-weighted images of $MnCO_3$@PDA NPs were brighter both in pH 7.4 and 6.0. These results demonstrate that $MnCO_3$ itself is an effective T_1 contrast agent with a r_1 value of 5.7 $mM^{-1}s^{-1}$, and the PDA coating could further induce a higher r_1 relaxivity of $MnCO_3$.

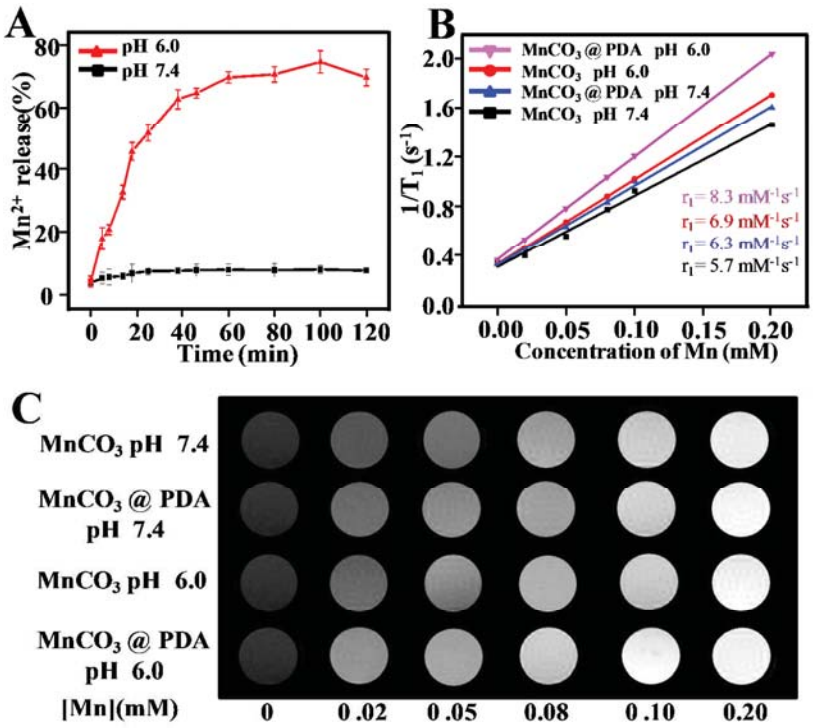

Figure 2. (A) Release profiles of Mn^{2+} from $MnCO_3$@PDA NPs in pH 7.4 and 6.0 within 120 min. (B) Linear relationship of R_1 ($1/T_1$) vs Mn concentration for $MnCO_3$ and $MnCO_3$@PDA

when they were immersed in pH 7.4 and 6.0. (C) T_1 weighted MR images of different Mn^{2+} concentrations in $MnCO_3$ and $MnCO_3$@PDA in pH 7.4 and 6.0.

3.3 Photothermal Conversion of NPs

Owing to the series of oxidation-reduction reaction happened in the process of self-polymerization of dopamine, the synthesized PDA appears to be a dark color in water.[52] Figure S8 showed the colorless solution of $MnCO_3$ dispersed in water (the left one), while once coated with PDA, the color of solution became yellow-brown (the right one). Importantly, UV/Vis spectra of $MnCO_3$ and $MnCO_3$@PDA NPs in Figure 3A revealed a broad absorption from visible to near-infrared light range (550~900 nm). Nevertheless, due to the coating of PDA, the absorption value of $MnCO_3$@PDA was higher than $MnCO_3$ at same concentration, indicating that $MnCO_3$@PDA could be applied as a potential candidate for photothermal therapy. Next we investigated the photothermal effect by monitoring the temperature of 0.5 mL water containing $MnCO_3$@PDA or $MnCO_3$ NPs under 808 nm NIR light irradiation. As shown in Figure 3B, temperature of $MnCO_3$@PDA solution (0.3 mg/mL) could reach up to 60 °C when irradiate with 808 nm (2 W/cm^2) laser device for 10 min while water and $MnCO_3$ NPs solution (0.3 mg/mL) showed little temperature change. Such excellent photothermal efficiency of $MnCO_3$@PDA mainly attributed to the coating of PDA. And the photothermal efficiency showed a great dependence on concentration of $MnCO_3$@PDA NPs. Furthermore, all the final temperature could reach to 60 °C after continuous irradiations with 808 nm lasers for three cycles, indicating a good photostability of $MnCO_3$@PDA NPs (Figure 3C). Figure 3D showed the infrared thermal images of water, $MnCO_3$ (0.3 mg/mL) and different concentrations (0.1-0.3 mg/mL) of $MnCO_3$@PDA NPs under continuous irradiation by an 808 nm laser for 10 min. It intuitively revealed the excellent photothermal performance of $MnCO_3$@PDA compared with $MnCO_3$ NPs, which

mainly attributed to the PDA coatings. And the photothermal efficiency of $MnCO_3$@PDA was dependent on the variation of concentration of $MnCO_3$@PDA NPs. Therefore, $MnCO_3$@PDA with high photothermal effect and good photostability is superior candidate for PTT.

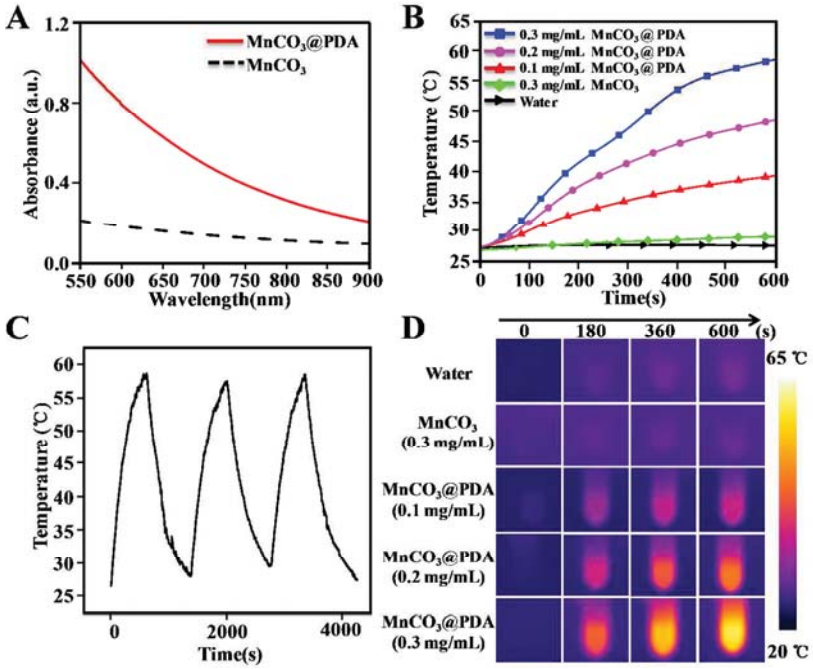

Figure 3. (A) Visible-NIR absorption spectra of $MnCO_3$ and $MnCO_3$@PDA NPs dispersion in water. (B) Temperature elevation of water, $MnCO_3$ (0.3 mg/mL) and different concentrations of $MnCO_3$@PDA NPs suspensions under continuous irradiation by an 808 nm laser with a power density of 2 W/cm^2 for 10 min. (C) Temperature variations of $MnCO_3$@PDA NPs under the continuous irradiations of 808 nm laser (2 W/cm^2) for three cycles. (D) Infrared thermal images of pure water, $MnCO_3$ (0.3 mg/mL) and different concentrations of $MnCO_3$@PDA NPs suspensions under continuous irradiation by an 808 nm laser.

3.4. In Vitro Cellular Uptake and Photothermal Cytotoxicity Evaluation

Before exploring the performance of $MnCO_3$@PDA NPs *in vivo*, bio-related experiment included cellular uptake and cellular toxicity had been investigated as follows. For cellular

uptake, FITC was used to fabricate a $MnCO_3$-PEI-FITC and $MnCO_3$@PDA-FITC fluorescence nanoprobe through the strong bond coupling between thiourea and amine group.[53] The confocal laser scanning microscopy (CLSM) imaging showed the successful endocytosis of FITC labeled $MnCO_3$-PEI NPs for the green fluorescence of FITC observed in HeLa cells (Figure S9). Additionally, the intracellular uptake of $MnCO_3$@PDA-FITC had also been investigated by increasing the incubation time from 1 to 8 h. After 8 h of incubation, the strongest fluorescence intensity of HeLa cells could be detected (Figure 4A.), while the fluorescence intensity at 12 h showed no obvious change, demonstrating that the highest cellular uptake of $MnCO_3$@PDA NPs may be arrived at 8 h after incubation with Hela cells.

For cellular toxicity, MTT assay was firstly used to examine the cytotoxicity of Mn^{2+} and CTAB before evaluating the biocompatibility of $MnCO_3$ and $MnCO_3$@PDA NPs. There were above 80 % HeLa cells alive when the concentration of Mn^{2+} was at 600 μM (Figure S10a), indicated that Mn^{2+} was relatively biocompatible when the concentration was below 600 μM, while CTAB exhibited a strong cytotoxicity even at a low concentration of 0.8 μM (Figure S10b). The biocompatible result of $MnCO_3$ and $MnCO_3$@PDA NPs had shown in Figure 4B. Obviously, only about 70 % HeLa cells alive at low the concentration (100 μg/mL), showing an obvious toxicity of $MnCO_3$ NPs. However, when coated with PDA shell, the cytotoxicity against HeLa cells was sharply dropped and there were about 85 % HeLa cells still alive even under the maximal experimental concentration of 300 μg/mL. Meanwhile, compared with $MnCO_3$ NPs, $MnCO_3$@PDA NPs also exhibited a relative lower toxicity to 4T1 cells (Figure S11). Additionally, the timescale toxicity of $MnCO_3$@PDA NPs had also been carried out by increasing the incubation time of $MnCO_3$@PDA NPs and HeLa cells (Figure S11). The cell viability of HeLa cells were more than 80% at the concentration range from 0 to 0.2 mg/mL

during the incubation time of 24-72 h, demonstrated a good biocompatibility of the $MnCO_3$@PDA NPs. Next, we investigated the photothermal ablation of cells with the existence of $MnCO_3$@PDA NPs by using laser irradiation (2 W/cm^2) for 10 min (Figure 4B and Figure S11). As expected, the cell viabilities decreased remarkably in a concentration-dependent manner after being dealt with $MnCO_3$@PDA NPs and laser irradiation. Furthermore, the fluorescence images of live/dead cell were obtained in figure 4C. A good growth state of HeLa cells was confirmed by the appearance of total vivid green fluorescence when they were cultured with medium only. Meanwhile, no obvious cell death was observed in the presence of laser irradiation, demonstrating the safety of 808 nm laser irradiation (2 W/cm^2) in our experiment. And the cells cultured with $MnCO_3$@PDA NPs showed a feeble red fluorescence, indicating a low cytotoxicity of $MnCO_3$@PDA NPs. In contrast, with the aid of the laser irradiation, the HeLa cells incubate with $MnCO_3$@PDA NPs showed almost complete red fluorescence, indicative of cell death. Such results were consistent with MTT test, and also suggested that the $MnCO_3$@PDA nanocomplex is an effective photothermal ablation agent to kill cancer cells.

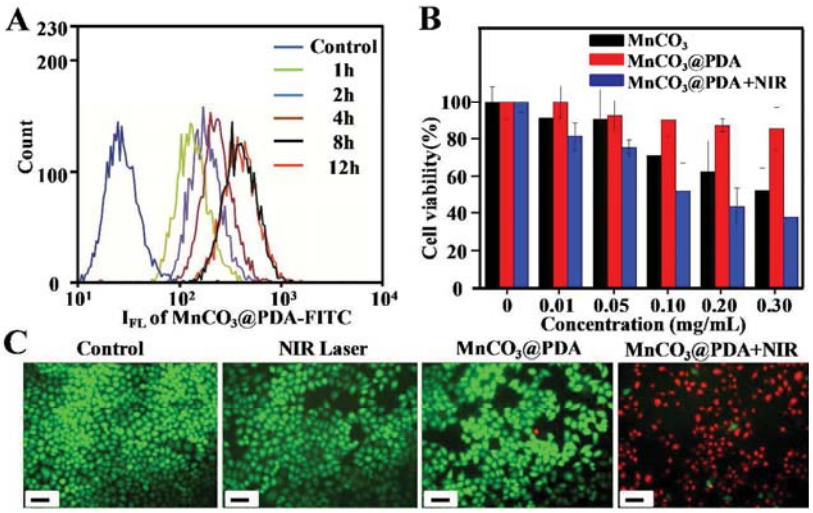

Figure 4. (A) Cellular uptake of $MnCO_3$@PDA at different time intervals. (B) Cell viability of HeLa cells incubated with $MnCO_3$, $MnCO_3$@PDA, and $MnCO_3$@PDA+NIR. (C) Fluorescence

images of HeLa cells stained with live/dead kit after in vitro photothermal ablation by 808 nm laser irradiation with and without the addition of $MnCO_3$@PDA NPs. Scale bar, 100 μm.

3.5. In Vivo MRI and Photothermal Ablation of $MnCO_3$@PDA NPs

To further verify the MR imaging results of $MnCO_3$@PDA *in vivo*, 4T1 xenograft tumor-bearing mouse was used to collect MR signals. As shown in Figure 5(A-G), a significantly bright MR image was obviously observed in the tumor site. And the images brighten gradually as time goes on. Similarity, it can be found that in the time course of post-injection, the relative T_1-weighted MRI signal value at tumor site was also increased and reached to a platform at about 70 minutes (Figure 5H), attributed to the dissolving and releasing out of free Mn^{2+} from $MnCO_3$@PDA in acidic environment. Such findings indicate that the pH-sensitive $MnCO_3$@PDA NPs could be used as effective contrast agents for MRI applications.

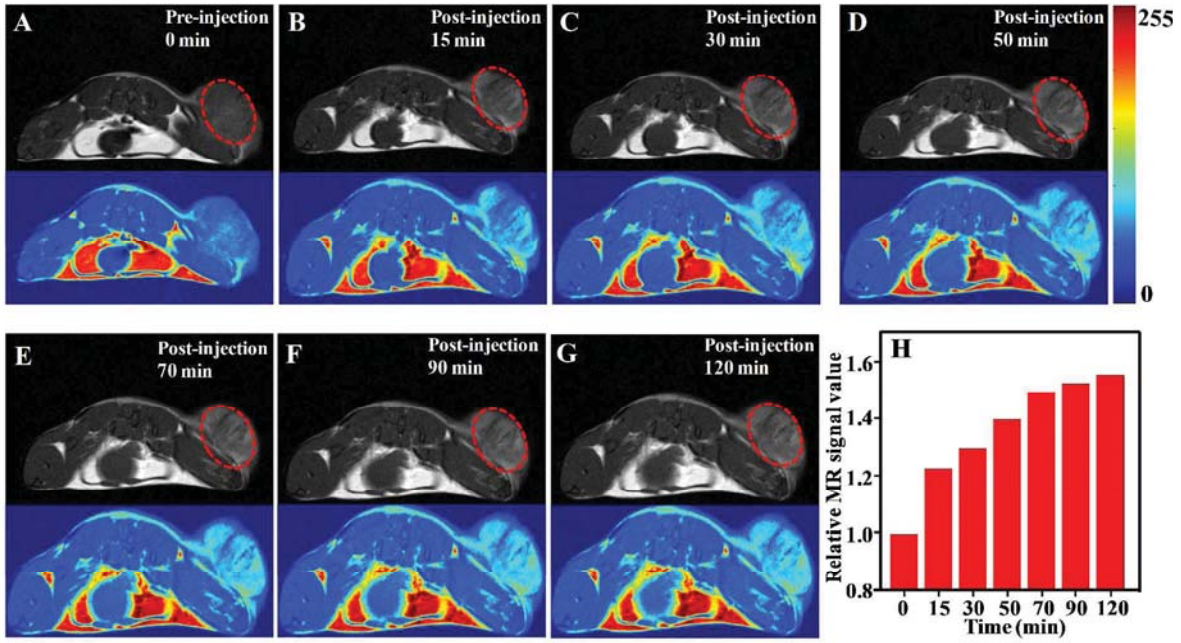

Figure 5. (A-G) *In vivo* T_1-weighed MR imaging of 4T1 tumor bearing-mouse at different time intervals after the intratumoral injection of $MnCO_3$@PDA NPs and the bottom one are their

respective color coded images. The red circles indicate tumor issues. (H) Corresponding normalized signal intensity of T_1-weighted MR signals from the tumor at different time.

Inspired by the excellent *in vitro* photothermal efficiency of $MnCO_3$@PDA NPs concluded by the above results, the *in vivo* photothermal ablation of cancer cells was next carried out on 4T1 tumor bearing-mice. In the process of experiment, mice had been randomly distributed into four groups (4 mice in each group) named as PBS; PBS + NIR; $MnCO_3$@PDA and $MnCO_3$@PDA + NIR. The temperature of mice at tumor site injected with PBS did not change too much. The highest temperature arrived at 40.8 °C, which would not hurt the tissue of tumor.[54] While the treatment group showed an evident temperature change, and the final temperature at tumor site was 55.8 °C after irradiation (1.4 W/cm^2) for 6 min (Figure 6A and 6B). The change in tumor size of mice was shown in Figure 6C and 6D, the groups treated with PBS, $MnCO_3$@PDA NPs and PBS + NIR showed rapid tumor growth, indicating that the $MnCO_3$@PDA NPs and laser irradiation did not affect the growth of tumor cells. However, the $MnCO_3$@PDA + NIR group caused complete ablation of the tumor. Besides, during the two weeks of treatment, no significant body weight change was observed in all groups (Figure 6E), showing that $MnCO_3$@PDA nanocomplex had no significant side effects on the treated mice.

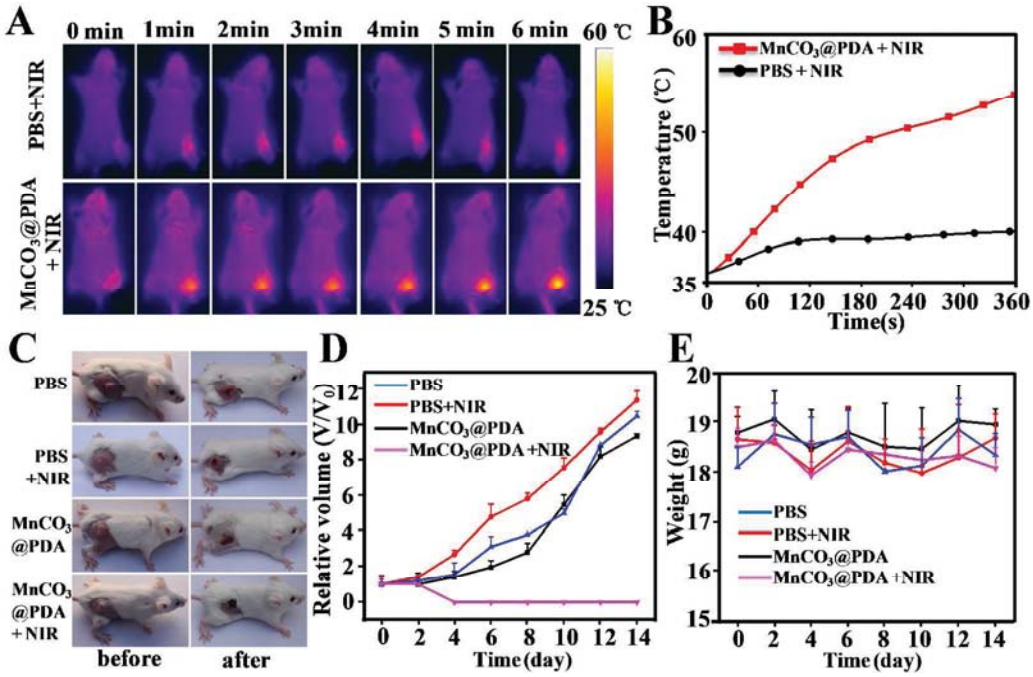

Figure 6. (A) IR thermal images of tumor-bearing mice with or without $MnCO_3$@PDA injection under exposure to the 808 nm laser (1.4 W/cm^2) recorded at different time intervals. (B) The temperature of tumor-bearing mice at tumor site with or without $MnCO_3$@PDA injection under exposure to the 808 nm laser. (C) Photos showing the change in tumors of the mice before and after treatment. (D) The change of relative tumor volume during treatment period. (E) Change of body weight during therapy.

Additionally, the *in vivo* PTT effect and potential toxicity of $MnCO_3$@PDA NPs were analyzed by H&E staining of tumors and major organs. Obviously, severe tumor damage with cell shrinkage, tumor necrosis and destroyed blood vessels was observed in the group treated with $MnCO_3$@PDA + NIR. But in contrast, the other groups dealt with PBS, $MnCO_3$@PDA NPs and PBS + NIR (Figure 7) showed little tumor destruction, indicating that PBS, $MnCO_3$@PDA NPs and NIR were harmless to cancer cells. Meanwhile, the H&E images of major organs from 4T1 tumor bearing mice in all groups showed no visible morphological change caused by NIR

laser, $MnCO_3$@PDA NPs or the PTT treatment compared with PBS group. These results further confirm that the $MnCO_3$@PDA NPs with excellent biocompatibility could be applied as a nanotheranostic agent for the future imaging guided PTT of cancer.

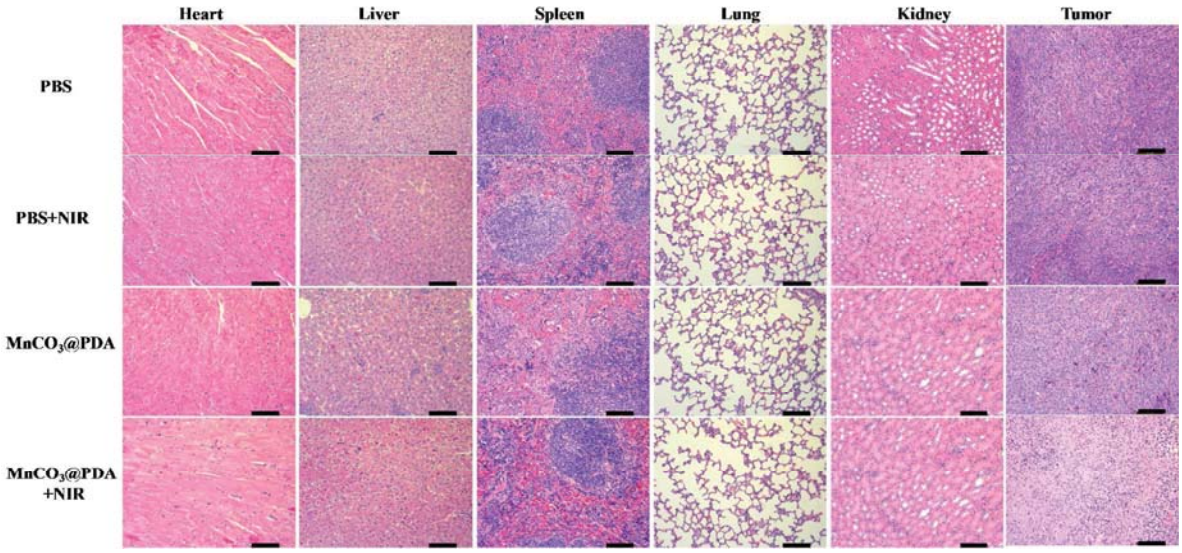

Figure 7. H&E stained images of heart, liver, spleen, lung, kidney and tumor collected from mice of various groups with different treatments after 14 days. Scale bar, 100 μm.

4. CONCLUSION

In summary, we have successfully designed and fabricated a biocompatible multifunctional core/shell $MnCO_3$@PDA nanotheranostic agent applied for MRI guided PTT. The as-synthesized $MnCO_3$@PDA NPs not only show excellent biocompatibility, high photothermal conversion efficiency but also exhibit outstanding MR contrast capabilities. Benefiting from PDA shell, the longitudinal relaxivity of $MnCO_3$ NPs was increased both in pH 7.4 and 6.0. The ultrahigh relaxivity (8.3 $mM^{-1}s^{-1}$) in the acidic condition ensures the nanoparticle an excellent contrast agent for MRI. Meanwhile, *in vitro* and *in vivo* experiment showed that the PDA shell not only plays an important role in photothermal conversion for PTT but also endows the nanoparticle with excellent biosecurity. These results demonstrate that the multifunctional

$MnCO_3$@PDA nanocomposite is expected to be used as a powerful theranostic agent for amplified magnetic resonance imaging guided photothermal therapy.

ASSOCIATED CONTENT

Supporting Information:

SEM image of $MnCO_3$ NPs; TEM images of $MnCO_3$ NPs, PAA modified $MnCO_3$ NPs and PDA coated $MnCO_3$ NPs; The SAED image of $MnCO_3$ NPs; XPS wide-scan survey spectra and N1s spectra of $MnCO_3$ and $MnCO_3$@PDA NPs; TG analysis of $MnCO_3$ without CTAB (synthesized by mixture of $MnCl_2$ and $(NH_4)_2CO_3$ solutions only), $MnCO_3$-CTAB and pure CTAB in N_2 atmosphere; TG analysis of $MnCO_3$-CTAB, $MnCO_3$-CTAB@PDA and PDA in air atmosphere. The stability of $MnCO_3$ and $MnCO_3$@PDA NPs investigated by DLS and Zeta potential; the color of $MnCO_3$ and $MnCO_3$@PDA NPs dispersed in water; CLSM images of HeLa cells after incubation with FITC labeled $MnCO_3$-PEI NPs; Cell viability of HeLa cells incubated with different concentration of $MnCl_2$ and CTAB for 24 h; Cell viability of 4T1 cells incubated with $MnCO_3$, $MnCO_3$@PDA, and $MnCO_3$@PDA + NIR; The Cell viability of HeLa cells incubated with $MnCO_3$@PDA NPs for 24, 36, 48 and 72 h.

AUTHOR INFORMATION

Corresponding Author

* Tel: +86-15359203806； Email: xizhou@xmu.edu.cn

* Tel: +86-13030892886； Email: chenzhiwei@xmu.edu.cn

Notes

The authors declare no competing financial interest.

ACKNOWLEDGMENT

This study was financially supported by the National Natural Science Foundation of China (31271071, 31371012, and U1505228).

REFERENCES

(1) Sumer, B.; Gao, J. M. Theranostic Nanomedicine for Cancer. *Nanomedicine* **2008,** *3*, 137-140.

(2) Horcajada, P.; Chalati, T.; Serre, C.; Gillet, B.; Sebrie, C.; Baati, T.; Eubank, J. F.; Heurtaux, D.; Clayette, P.; Kreuz, C.; Chang, J. S.; Hwang, Y. K.; Marsaud, V.; Bories, P. N.; Cynober, L.; Gil, S.; Ferey, G.; Couvreur, P.; Gref, R. Porous Metal-Organic-Framework Nanoscale Carriers as a Potential Platform for DrugDelivery and Imaging. *Nat. mater.* **2010,** *9*, 172-178.

(3) Cai, X. J.; Gao, W.; Ma, M.; Wu, M. Y.; Zhang, L. L.; Zheng, Y. Y.; Chen, H. R.; Shi, J. L. A Prussian Blue-Based Core-Shell Hollow-Structured Mesoporous Nanoparticle as a Smart Theranostic Agent with Ultrahigh pH-Responsive Longitudinal Relaxivity. *Adv. Mater.* **2015,** *27*, 6382-6389.

(4) Kairdolf, B. A.; Qian, X.; Nie, S. Bioconjugated Nanoparticles for Biosensing, In-Vivo Imaging, and Medical Diagnostics. *Anal. Chem.* **2017,** *89*, 1015-1031.

(5) Anselmo, A. C.; Mitragotri, S. A Review of Clinical Translation of Inorganic Nanoparticles. *AAPS J.* **2015,** *17*, 1041-1054.

(6) Mo, A. H.; Zhang, C.; Landon, P. B.; Janetanakit, W.; Hwang, M. T.; Gomez, K. S.; Colburn, D. A.; Dossou, S. M.; Lu, T.; Cao, Y.; Sant, V.; Sud, P. L.; Akkiraju, S.; Shubayev, V. I.; Glinsky, G.; Lal, R. Dual-Functionalized Theranostic Nanocarriers. *ACS Appl. Mater. Interfaces* **2016,** *8*, 14740-14746.

(7) Zeng, Y. Y.; Zhang, D.; Wu, M.; Liu, Y.; Zhang, X.; Li, L.; Li, Z.; Han, X.; Wei, X. Y.; Liu, X. L. Lipid-AuNPs@PDA Nanohybrid for MRI/CT Imaging and Photothermal Therapy of Hepatocellular Carcinoma. *ACS Appl. Mater. Interfaces* **2014,** *6*, 14266-14277.

(8) Kang, N.; Liu, Y.; Zhou, Y. M.; Wang, D.; Chen, C.; Ye, S. F.; Nie, L. M.; Ren, L. Phase and Size Control of Core-Shell Upconversion Nanocrystals Light Up Deep Dual Luminescence Imaging and CT In Vivo. *Adv. Healthcare Mater.* **2016,** *5*, 1356-1363.

(9) Wen, L.; Chen, L.; Zheng, S. M.; Zeng, J. F.; Duan, G. G.; Wang, Y.; Wang, G. G.; Chai, Z. F.; Li, Z.; Gao, M. Y. Ultrasmall Biocompatible WO_{3-x} Nanodots for Multi-Modality Imaging and Combined Therapy of Cancers. *Adv. Mater.* **2016,** *28*, 5072-5079.

(10) Dou, Y.; Li, X.; Yang, W. T.; Guo, Y. Y.; Wu, M. L.; Liu, Y. J.; Li, X. D.; Zhang, X. N.; Chang, J. PB@Au Core-Satellite Multifunctional Nanotheranostics for Magnetic Resonance and Computed Tomography Imaging in Vivo and Synergetic Photothermal and Radiosensitive Therapy. *ACS Appl. Mater. Interfaces* **2017,** *9*, 1263-1272.

(11) Yang, G. B.; Gong, H.; Liu, T.; Sun, X. Q.; Cheng, L.; Liu, Z. Two-Dimensional Magnetic WS_2@Fe_3O_4 Nanocomposite with Mesoporous Silica Coating for Drug Delivery and Imaging-Guided Therapy of Cancer. *Biomaterials* **2015,** *60*, 62-71.

(12) Jin, Y. S.; Li, Y. Y.; Ma, X. B.; Zha, Z. B.; Shi, L. L.; Tian, J.; Dai, Z. F. Encapsulating Tantalum Oxide into Polypyrrole Nanoparticles for X-ray CT/Photoacoustic Bimodal Imaging-Guided Photothermal Ablation of Cancer. *Biomaterials* **2014,** *35*, 5795-5804.

(13) Bauman, G.; Johnson, K. M.; Bell, L. C.; Velikina, J. V.; Samsonov, A. A.; Nagle, S. K.; Fain, S. B. Three-Dimensional Pulmonary Perfusion MRI with Radial Ultrashort Echo Time and Spatial-Temporal Constrained Reconstruction. *Magn. Reson. Med.* **2015,** *73*, 555-564.

(14) Ryo, I.; Tomohiro, N.; Syutaro, A.; Kazuhiro, K.; Yasuyuki, Y. Clinical Application of Navigator-Gated Three-Dimensional Balanced Turbo-Field-Echo Magnetic Resonance Cholangiopancreatography at 3 T: Prospective Intraindividual Comparison with 1.5 T. *Abdo. Radio.* **2016,** *41*, 1285-1292.

(15) Jaque, D.; Maestro, L. M.; Rosal, B. d.; Gonzalez, P. H.; Benayas, A.; Plaza, J. L.; Rodriguez, E. M.; Sole, J. G. Nanoparticles for Photothermal Therapies. *Nanoscale* **2014,** *6*, 9494-9530.

(16) Shanmugam, V.; Selvakumar, S.; Yeh, C. S. Near-Infrared Light-Responsive Nanomaterials in Cancer Therapeutics. *Chem. Soc. Rev.* **2014,** *43*, 6254-6287.

(17) Chen, Z. W.; Jiao, Z.; Pan, D. Y.; Li, Z.; Wu, M. H.; Shek, C.-H.; Wu, C. M. L.; Lai, J. K. L. Recent Advances in Manganese Oxide Nanocrystals: Fabrication, Characterization, and Microstructure. *Chem. Rev.* **2012,** *112*, 3833-3855.

(18) Li, X. W.; Zhao, W. R.; Liu, X. H.; Chen, K. Q.; Zhu, S. J.; Shi, P.; Chen, Y.; Shi, J. L. Mesoporous Manganese Silicate coated Silica Nanoparticles as Multi-Stimuli-Responsive T_1-MRI Contrast Agents and Drug Delivery Carriers. *Acta Biomater.* **2016,** *30*, 378-387.

(19) Zhang, Y.; Tan, J. Q.; Long, M.; Yang, H. M.; Yuan, S. W.; Tang, A. D.; Chang, S.; Hu, Y. H. An Emerging Dual Collaborative Strategy for High-Performance Tumor Therapy with Mesoporous Silica Nanotubes Loaded with Mn_3O_4. *J. Mater. Chem. B* **2016,** *4*, 7406-7414.

(20) Tseng, Y.-J.; Chou, S.-W.; Shyue, J.-J.; Lin, S.-Y.; Hsiao, J.-K.; Chou, P.-T. A Versatile Theranostic Delivery Platform Integrating Magnetic Resonance Imaging/Computed Tomography, pH/cis-Diol Controlled Release, and Targeted Therapy. *ACS Nano* **2016,** *10*, 5809-5822.

(21) Howell, M.; Mallela, J.; Wang, C.; Ravi, S.; Dixit, S.; Garapati, U.; Mohapatra, S. Manganese-Loaded Lipid-Micellar Theranostics for Simultaneous Drug and Gene Delivery to Lungs. *J. Controlled Release* **2013,** *167*, 210-218.

(22) Schladt, T. D.; Schneider, K.; Shukoor, M. I.; Natalio, F.; Bauer, H.; Tahir, M. N.; Weber, S.; Schreiber, L. M.; Schröder, H. C.; Müller, W. E. G.; Tremel, W. Highly Soluble Multifunctional MnO Nanoparticles for Simultaneous Optical and MRI Imaging and Cancer Treatment Using Photodynamic Therapy. *J. Mater. Chem.* **2010,** *20*, 8297-8304.

(23) Wang, S.; Zhang, Q.; Yang, P.; Yu, X. R.; Huang, L. Y.; Shen, S.; Cai, S. J. Manganese Oxide-Coated Carbon Nanotubes As Dual-Modality Lymph Mapping Agents for Photothermal Therapy of Tumor Metastasis. *ACS Appl. Mater. Interfaces* **2016,** *8*, 3736-3743.

(24) Zhang, M.; Cao, Y.; Wang, L.; Ma, Y.; Tu, X.; Zhang, Z. Manganese Doped Iron Oxide Theranostic Nanoparticles for Combined T_1 Magnetic Resonance Imaging and Photothermal Therapy. *ACS Appl. Mater. Interfaces* **2015,** *7*, 4650-4658.

(25) Liu, R. F.; Jing, L. J.; Peng, D.; Li, Y.; Tian, J.; Dai, Z. F. Manganese(II) Chelate Functionalized Copper Sulfide Nanoparticles for Efficient Magnetic Resonance/Photoacoustic Dual-Modal Imaging Guided Photothermal Therapy. *Theranostics* **2015,** *5*, 1144-1153.

(26) Shin, T. H.; Choi, Y.; Kim, S.; Cheon, J. Recent Advances in Magnetic Nanoparticle-Based Multi-Modal Imaging. *Chem. Soc. Rev.* **2015,** *44*, 4501-4516.

(27) Peng, Y.-K.; Lai, C.-W.; Liu, C.-L.; Chen, H.-C.; Hsiao, Y.-H.; Liu, W.-L.; Tang, K.-C.; Chi, Y.; Hsiao, J.-K.; Lim, K.-E.; Liao, H.-E.; Shyue, J.-J.; Chou, P.-T. A New and Facile Method To Prepare Uniform Hollow MnO/Functionalized mSiO_2 Core/Shell Nanocomposites. *ACS Nano* **2011,** *5*, 4177-4187.

(28) Shin, J. M.; Anisur, R. M.; Ko, M. K.; Im, G. H.; Lee, J. H.; Lee, I. S. Hollow Manganese Oxide Nanoparticles as Multifunctional Agents for Magnetic Resonance Imaging and Drug Delivery. *Angew. Chem. Int. Ed.* **2009,** *48*, 321-324.

(29) Park, M.; Lee, N.; Choi, S. H.; An, K.; Yu, S.-H.; Kim, J. H.; Kwon, S.-H.; Kim, D.; Kim, H.; Baek, S.-I.; Ahn, T.-Y.; Park, O. K.; Son, J. S.; Sung, Y. E.; Kim, Y. W.; Wang, Z. W.; Pinna, N.; Hyeon, T. Large-Scale Synthesis of Ultrathin Manganese Oxide Nanoplates and Their Applications to T_1 MRI Contrast Agents. *Chem. Mater.* **2011,** *23*, 3318-3324.

(30) Huang, J.; Xie, J.; Chen, K.; Bu, L. H.; Lee, S.; Cheng, Z.; Li, X. G.; Chen, X. Y. HSA Coated MnO Nanoparticles with Prominent MRI Contrast for Tumor Imaging. *Chem. Commun.* **2010,** *46*, 6684-6686.

(31) Shao, C.; Li, S.; Gu, W.; Gong, N. Q.; Zhang, J.; Chen, N.; Shi, X. Y.; Ye, L. Multifunctional Gadolinium-Doped Manganese Carbonate Nanoparticles for Targeted MR/Fluorescence Imaging of Tiny Brain Gliomas. *Anal. Chem.* **2015,** *87*, 6251-6257.

(32) Liu, Y. L.; Ai, K. L.; Lu, L. H. Polydopamine and Its Derivative Materials: Synthesis and Promising Applications in Energy, Environmental, and Biomedical Fields. *Chem. Rev.* **2014,** *114*, 5057-5115.

(33) Shao, L. H.; Zhang, R. R.; Lu, J. Q.; Zhao, C. Y.; Deng, X. W.; Wu, Y. Mesoporous Silica Coated Polydopamine Functionalized Reduced Graphene Oxide for Synergistic Targeted Chemo-Photothermal Therapy. *ACS Appl. Mater. Interfaces* **2017,** *9*, 1226-1236.

(34) Perikamana, S. K. M.; Lee, J.; Lee, Y. B.; Shin, Y. M.; Lee, E. J.; Mikos, A. G.; Shin, H. Materials from Mussel-Inspired Chemistry for Cell and Tissue Engineering Applications. *Biomacromolecules* **2015,** *16*, 2541-2555.

(35) Liu, M., Ying.; Zeng, G., Jian.; Wang, K.; Wan, Q.; Tao, L.; Zhang, X., Yong.; Wei, Y. Recent Developments in Polydopamine: An Emerging Soft Matter for Surface Modification and Biomedical Applications. *Nanoscale* **2016,** *8*, 16819-16840.

(36) Liu, Y. L.; Ai, K. L.; Liu, J. H.; Deng, M.; He, Y. Y.; Lu, L. H. Dopamine-Melanin Colloidal Nanospheres: An Efficient Near-Infrared Photothermal Therapeutic Agent for In *Vivo* Cancer Therapy. *Adv. Mater.* **2013,** *25*, 1353-1359.

(37) Lin, L. S.; Cong, Z. X.; Cao, J. B.; Ke, K. M.; Peng, Q. L.; Gao, J. H.; Yang, H. H.; Liu, G.; Chen, X. Y. Multifunctional Fe_3O_4@Polydopamine Core-Shell Nanocomposites for Intracellular mRNA Detection and Imaging-Guided Photothermal Therapy. *ACS Nano* **2014,** *8* 3876-3883.

(38) Liu, F. Y.; He, X. X.; Lei, Z.; Liu, L.; Zhang, J. P.; You, H. P.; Zhang, H. M.; Wang, Z. X. Facile Preparation of Doxorubicin-Loaded Upconversion@Polydopamine Nanoplatforms for Simultaneous In Vivo Multimodality Imaging and Chemophotothermal Synergistic Therapy. *Adv. Healthcare Mater.* **2015,** *4*, 559-568.

(39) Liu, D. D.; Ma, L. Y.; Liu, L. D.; Wang, L.; Liu, Y. X.; Jia, Q.; Guo, Q. W.; Zhang, G.; Zhou, J. Polydopamine-Encapsulated Fe_3O_4 with an Adsorbed HSP70 Inhibitor for Improved Photothermal Inactivation of Bacteria. *ACS Appl. Mater. Interfaces* **2016,** *8*, 24455-24462.

(40) Cui, J. W.; Yan, Y.; Such, G. K.; Liang, K.; Ochs, C. J.; Postma, A.; Caruso, F. Immobilization and Intracellular Delivery of an Anticancer Drug Using Mussel-Inspired Polydopamine Capsules. *Biomacromolecules* **2012,** *13*, 2225-2228.

(41) Westen, R. V. d.; Hosta-Rigau, L.; Sutherland, D. S.; Goldie, K. N.; Albericio, F.; Postma, A.; Stadler, B. Myoblast Cell Interaction with Polydopamine Coated Liposomes. *Biointerphases* **2012,** *7*, 1-9.

(42) Liu, K.; Shi, X.; Wang, T. J.; Ai, P. H.; Gu, W.; Ye, L. Terbium-Doped Manganese Carbonate Nanoparticles With Intrinsic Photoluminescence and Magnetic Resonance Imaging Capacity. *J. Colloid Interface Sci.* **2017,** *485*, 25-31.

(43) Wu, X. L.; Cao, M. H.; Lü, H. Y.; He, X. Y.; Hu, C. W. Microemulsion-Mediated Solvothermal Synthesis and Morphological Evolution of $MnCO_3$ Nanocrystals. *J. Nanosci. Nanotechnol.* **2006,** *6*, 2123-2128.

(44) Zheng, R.; Wang, S.; Ye Tian; Xing Guo Jiang; De Liang Fu; Shen, S.; Yang, W. L. Polydopamine-Coated Magnetic Composite Particles with an Enhanced Photothermal Effect. *ACS Appl. Mater. Interfaces* **2015,** *7*, 15876-15884.

(45) Miao, Z. H.; Wang, H.; Yang, H.; Li, Z. L.; Zhen, L.; Xu, C. Y. Intrinsically Mn^{2+}-Chelated Polydopamine Nanoparticles for Simultaneous Magnetic Resonance Imaging and Photothermal Ablation of Cancer Cells. *ACS Appl. Mater. Interfaces* **2015,** *7*, 16946-16952.

(46) Gadaleta, S. J.; Paschalis, E. P.; Betts, F.; Mendelsohn, R.; Boskey, A. L. Fourier Transform Infrared Spectroscopy of The Solution-Mediated Conversion of Amorphous Calcium Phosphate to Hydroxyapatite: New Correlations Between X-ray Diffraction and Infrared Data. *Galcified Tissue Inter.* **1996,** *58*, 9-16.

(47) Fu, Q. F.; Li, X. J.; Zhang, Q. H.; Yang, F. Q.; Wei, W. L.; Xia, Z. N. A Facile and Versatile Approach for Controlling Electroosmotic Flow in Capillary Electrophoresis via Mussel Inspired Polydopamine/Polyethyleneimine Co-deposition. *J. Chromatogr. A* **2015,** *1416*, 94-102.

(48) Lin, H. Z.; Deng, C. H. Development of Hf^{4+}-Immobilized Polydopamine-Coated Magnetic Graphene for Highly Selective Enrichment of Phosphopeptides. *Talanta* **2016,** *149*, 91-97.

(49) Lelli, M.; Roveri, N.; Marzano, C.; Hoeschele, J. D.; Curci, A.; Margiotta, N.; Gandin, V.; Natile, G. Hydroxyapatite Nanocrystals as a Smart, pH Sensitive, Delivery System for Kiteplatin. *Dalton Trans.* **2016,** *45*, 13187-13195.

(50) Kim, D.; Lee, E. S.; Oh, K. T.; Gao, Z. G.; Bae, Y. H. Doxorubicin-Loaded Polymeric Micelle Overcomes Multidrug Resistance of Cancer by Double-Targeting Folate Receptor and Early Endosomal pH. *Small* **2008,** *4*, 2043-2050.

(51) Luo, Y. X.; Millero, F. J. Solubility of Rhodochrosite ($MnCO_3$) in NaCl Solutions. *J. Solution Chem.* **2003,** *32*, 405-416.

(52) Sureshkumar, M.; Lee, P.-N.; Lee, C.-K. Stepwise Assembly of Multimetallic Nanoparticles via Self-Polymerized Polydopamine. *J. Mater. Chem.* **2011,** *21*, 12316-12320.

(53) Lia, H.; Jia, Y.; Feng, X. Y.; Li, J. B. Facile Fabrication of Robust Polydopamine Microcapsules for Insulin Delivery. *J. Colloid Interface Sci.* **2017,** *487*, 12-19.

(54) Rotiroti, J. L. Cellular Responses to Hyperthermia (40-46 °C): Cell killing and Molecular Events. *Int. J. Hyperthermia* **2008,** *24*, 3-15.

Table of Contents